Charge-Selective Surface-Enhanced Raman Scattering Using Silver and Gold Nanoparticles Deposited on Silicon–Carbon Core–Shell Nanowires

Sun Young Baik,[†] Yong Jae Cho,[†] Young Rok Lim,[†] Hyung Soon Im,[†] Dong Myung Jang,[†] Yoon Myung,[†] Jeunghee Park,[†,*] and Hong Seok Kang[‡,*]

[†]Department of Chemistry, Korea University, Jochiwon Chungnam 339-700, Korea and [‡]Department of Nano and Advanced Materials, College of Engineering, Jeonju University, Chonju, Chonbuk 560-759, Korea

ABSTRACT The deposition of silver (Ag) or gold (Au) nanoparticles (NPs) on vertically aligned silicon–carbon (Si–C) core–shell nanowires (NWs) produces sensitive substrates for surface-enhanced Raman spectroscopy (SERS). The undoped and 30% nitrogen (N)-doped graphitic layers of the C shell (avg thickness of 20 nm) induce a higher sensitivity toward negatively (−) and positively (+) charged dye molecules, respectively, showing remarkable charge selectivity. The Ag NPs exhibit higher charge selectivity than the Au NPs. The Ag NPs deposited on p- and n-type Si NWs also exhibit (−) and (+) charge selectivity, respectively, which is higher than that of the Au NPs. The X-ray photoelectron spectroscopy analysis indicates that the N-doped graphitic layers donate more electrons to the metal NPs than the undoped ones. More distinct electron transfer occurs to the Ag NPs than to the Au NPs. First principles calculations of the graphene–metal adducts suggest that the large electron transfer capacity of the N-doped graphitic layers is due to the formation of a N→Ag coordinate bond involving the lone pair electrons of the N atoms. We propose that the more (−) charged NPs on the N-doped graphitic layers prefer the adsorption of (+) charged dyes, enhancing the SERS intensity. The charge selectivity of the Si NW substrates can also be rationalized by the greater electron transfer from the n-type Si to the metal NPs.

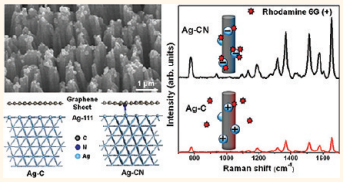

KEYWORDS: surface-enhanced Raman scattering · charge selectivity · N-doped graphitic layers · silicon nanowires · silver nanoparticles · first principles calculations · electron transfer

Raman spectroscopy is an important and powerful tool for characterizing the structures of materials. The Raman signal is enhanced by several orders of magnitude for molecules adsorbed onto the roughened surfaces or nanoparticles (NPs) of Ag or Au metal.[1−5] The origin of surface-enhanced Raman scattering (SERS) effect is still in dispute but may be attributed to two possible sources: the electromagnetic mechanism (EM), which is based on surface plasmon resonance (a factor of 10^6–10^8 enhancement), and the chemical mechanism (CM), which is based on charge transfer between the molecule and the substrate (usually a factor of 10–10^2 enhancement). The EM is believed to be due to the excitation of the localized surface plasmon resonance (LSPR), which greatly strengthens the electromagnetic field near the metal surface. To increase the SERS signal, the substrate should possess a huge surface area, in order to adsorb more target molecules, and abundant "hot" sites of metal NPs. Recently, aligned one-dimensional nanostructure arrays, such as Si nanowires (NWs), ZnO NWs, and carbon nanotubes (CNTs), have been frequently employed as sensitive SERS substrates.[6−16] A significant advantage of the aligned NW geometry is that it offers multiple reflections along the surface and strong pump beam absorption.

This SERS technique would be a more powerful analytical method if the selective adsorption of the analyte target could be achieved by controlling the charge of the metal NPs. Bhatt *et al.* reported that Ag NPs on n- and p-type Si wafers exhibit enhanced SERS for positively (acridine orange) and negatively (fluorescein) charged dye molecules, respectively.[17] Consistent with this report, Panarin *et al.* showed that Ag NP deposited n-type porous Si nanostructures are more sensitive SERS-active substrates than the corresponding p-type Si ones for positively charged Rhodamine 6G dye.[18] However, there have been few reports on the charge selective SERS of NW substrates.

* Address correspondence to parkjh@korea.ac.kr, hsk@jj.ac.kr.

Received for review December 8, 2011 and accepted February 8, 2012.

Published online February 08, 2012
10.1021/nn204797b

Recently, graphene, a new class of two-dimensional carbon nanostructures, has been considered as an excellent SERS substrate for absorbed species owing to its efficient quenching of the interfering excited-state luminescence.[19−24] Such an enhancement is believed to be caused by the electron transfer between the graphene and the molecule adsorbed on the surface (*i.e.*, CM). On the other hand, either placing graphene on a metal film or depositing (or decorating) NPs on graphene induces a large EM effect in the Raman signal of graphene.[25−29] Deposition of the NPs on the graphene (or graphene oxide) sheets can also be effectively used for the detection of low concentration molecules.[30−34] Therefore, the SERS of the NP deposited graphene substrates would provide an important insight for the coexistence of the EM and CM effects among the NPs, graphene sheets, and the adsorbed analytes.

Herein, we demonstrate sensitive and charge-selective SERS substrates, which were fabricated by depositing Ag or Au NPs on silicon−carbon (Si−C) core−shell NWs. The graphitic layers of the C shell were doped with 30% of N atoms, exclusively with a pyridine-like structure, using chemical vapor deposition (CVD).[35] Successive ion layer adsorption and reaction (SILAR) methods were developed to deposit the NPs with a controlled size. Remarkably, the undoped and N-doped graphitic layers induce greater charge selectivity of SERS toward negatively (−) and positively (+) charged dyes, respectively. The Ag NPs exhibit higher charge selectivity than the Au NPs. NP deposited p- and n-type Si NWs were also prepared as sensitive SERS substrates by the same SILA method, in order to examine their charge selectivity. We observed that the doping of the Si NWs and the graphitic layer sheathed Si NWs induce excellent charge selectivity.

To gain insight into the charge selectivity of the graphitic layers, we calculated the electronic structures of the graphene sheets adsorbed on the Ag(111) and Au(111) surfaces, using the first principles method. The graphene sheet effectively models the 20 nm thick graphitic layers with a large diameter (*ca.* 120 nm).[35] The binding energy suggests that the lone pair electrons of the pyridine-like motives play a role in producing the coordinate bonds along the direction perpendicular to the graphene plane, which induces more (−) charged metal NPs. We propose a model in which the more (−) charged NPs prefer the adsorption of (+) charged dyes, enhancing the SERS intensity. To the best of our knowledge, this is the first experimental and theoretical investigation of charge-selective SERS for graphitic layers.

RESULTS AND DISCUSSION

Fabrication of SERS Substrates. The average length of the Si NWs is 7 μm, and their average diameter is 80 nm.

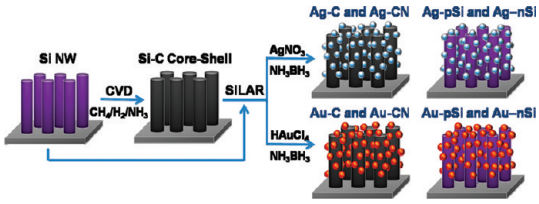

Scheme 1. Schematic diagram for the growth of Si−C NWs and the deposition of the metal NPs, producing the charge-selective SERS substrates (Ag−C, Ag−CN, Au−C, Au−CN; Ag−pSi, Ag−nSi, Au−pSi, Au−nSi)

The undoped and 30% N-doped graphitic layers sheathed the Si NW with a thickness of 20 nm. We refer to these Si−C core−shell NW substrates before the deposition of the NPs as C (undoped) and CN (N-doped) using the SILA method, respectively. We denote the Ag and Au NP deposited samples as Ag−C, Ag−CN, Au−C, and Au−CN hereafter. The 30% N doping of the graphitic layers was controlled selectively to be in pyridine-like N structures, as discussed below. Ag and Au NPs were also deposited on the p-type Si and n-type Si NWs and are referred to as Ag−pSi, Ag−nSi, Au−pSi, and Au−nSi hereafter. Scheme 1 describes the growth of NW and the deposition of the metal NPs to prepare the SERS substrates.

Figure 1a,b shows the typical SEM images of the Ag and Au NPs deposited on the vertically aligned Si−C NWs, respectively. The size of the Ag and Au NPs is distributed over a wide range of 5−70 nm. The size of the NPs on the tip is usually larger (30−70 nm) than that on the wall (5−10 nm). Figure 1c shows the corresponding high-resolution TEM (HRTEM) images for a selected Ag−C sample. The C shell consisted of randomly oriented graphitic layers whose (002) planes are separated by a distance of 3.4 Å (avg). The Ag NPs (size = 5−10 nm) are firmly attached to these crystalline graphitic layers. The lattice-resolved TEM and its corresponding fast Fourier transformed (FFT) images (zone axis of Ag = [011]) are shown in Figure 1d. The adjacent (111) planes of Ag are separated by 2.4 Å, which is consistent with that of face-centered cubic (fcc) Ag (JCPDS No. 87-0720; a = 4.077 Å). The EDX data confirm the presence of Ag, C, and Si elements (inset).

Figure 1e shows a typical SEM image of the Ag NP deposited Si NW substrates. Figure 1f shows their corresponding HRTEM and FFT images. The size of the NPs is 5−30 nm. The NPs on the wall have a smaller size than that on the tip, with an average value of 7 nm. The highly crystalline Ag NPs adhered tightly to the Si NW surface. The Si (200) fringes, perpendicular to the wire axis, are separated by a distance of about 2.7 Å, which is close to that of fcc Si (JCPDS No. 80-0018; a = 5.392 Å). The FFT image of the Si core part at the [011] zone axis confirms the presence of single-crystalline Si with the [100] direction along the axis (inset). The SEM and TEM images and EDX data of Au−C and Au−Si samples are provided in the Supporting Information (SI), Figure S1.

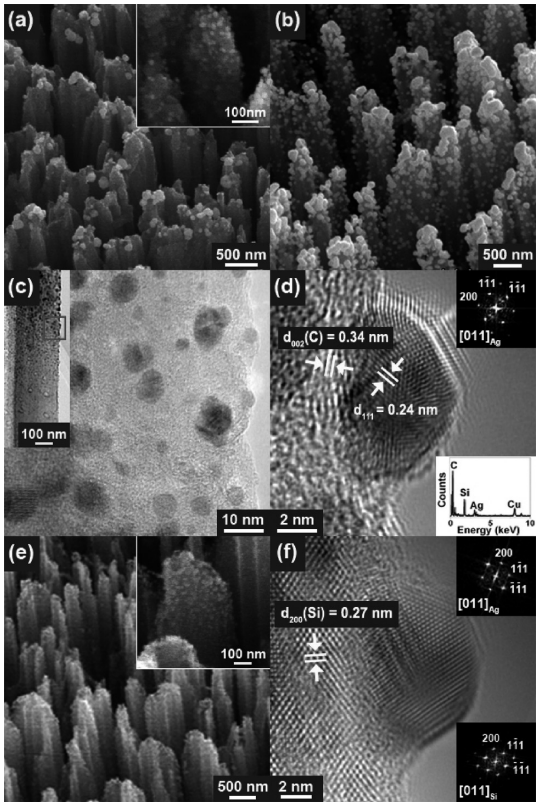

Figure 1. SEM micrograph of the (a) Ag NPs and (b) Au NPs deposited on the vertically aligned Si−C (20 nm thick C shell) NWs. (c) HRTEM images showing the Ag NPs attached to the graphitic layers (on the wall) with a size of 5−10 nm. (d) Lattice-resolved TEM and the corresponding FFT images (zone axis for Ag = [011]). The adjacent (111) planes of Ag NPs are separated by 2.4 Å. The EDX data confirm the presence of Ag, C, and Si elements (inset). (e) Typical SEM image for the Ag NP deposited Si NWs. (f) HRTEM and FFT (zone axis = [011] for both Ag and Si) images showing highly crystalline Ag NPs attached to the single-crystalline Si NWs having the [100] direction along the axis.

The main advantage of the SILAR method over other deposition processes is that it offers a simple and low-cost fabrication methodology and is analogous with the atomic layer deposition method.[36,37] We used AB since it provides better control over the size and density compared to that of other reducers such $NaBH_4$ and trisodium citrate. This result is consistent with that of previous works that amines can simultaneously act as a stabilizer when preparing SERS-active Ag and Au films on substrates.[38] As the concentration of the precursors and reducing reagent (AB) or the number of immersing cycles increases, the size and density of the NPs is usually increased. We fix the cycle number (20 cycles) for all substrates. As shown above, the size and density of the NPs is not homogeneous over the top and wall parts of the NW. The average size of Ag NPs is usually larger than that of Au NPs. The NPs on the Si NW have a smaller size than those on the Si−C core−shell NWs, and their density is higher. However, the size and density are nearly the same for a given pair of substrates; Ag−C *versus* Ag−CN, Au−C *versus* Au−CN, Ag−pSi *versus* Ag−nSi, Au−pSi *versus* Ai−nSi. Therefore, we were able to compare the relative SERS intensity of the paired substrates with high reproducibility, as shown below.

Charge-Selective SERS of Ag and Au NP Deposited NWs. In order to study the charge-selective SERS, aqueous solutions of two (+) charged dyes, Rhodamine 6G (R6G) and acridine orange (AO), and two (−) charged dyes, fluorescein (FL) and methyl orange (MO), were used. Figure 2 shows the SERS of R6G, AO, FL, and MO for the Ag−C and Ag−CN samples recorded under the same conditions, where the concentration is 10^{-6} M, the acquisition time is 1 s, and the laser power = 0.7 mW. For the (+) charged dyes, the Ag−CN exhibits an approximately 4 times higher intensity than the Ag−C. On the other hand, for the (−) charged dyes, the Ag−C demonstrates 10 times higher intensity than the Ag−CN. We measured the SERS as a function of the dye concentration and estimated the detection limit, as shown in the SI, Figures S2 and S3. Table S1 (SI) lists the detection limits (S/N = 3) of all four dyes, in the range of 10^{-10} to 10^{-15} M. For instance, the detection limit of Ag−CN is 2×10^{-15} M for R6G, while that of Ag−C is 3.2×10^{-13} M. The detection limits of Ag−C and Ag−CN differ by a factor of 10^2−10^4, confirming their charge selectivity. Figure 3 displays the SERS of R6G, AO, FL, and MO for the Au−C and Au−CN recorded under the same conditions. The Au−CN exhibits a higher intensity than the Au−C toward the (+) charged dyes, while the opposite is true for the (−) charged dyes. However, the charge selectivity of the Au NPs is noticeably less than that of the Ag NPs. We estimated the detection limit from the dependence of the intensity on the concentration (see SI, Figure S4). The detection limit is higher concentration than that of the Ag NPs, with the lower charge selectivity (see Table S1).

Figure 4 shows the SERS of R6G, AO, FL, and MO for the Ag−pSi and Ag−nSi recorded under the same conditions. The Au NPs on the p-type Si and n-type Si show selectivity toward the (−) and (+) charged dyes, respectively. For the (+) charged R6G and AO, the Ag−nSi exhibits 2 and 10 times higher intensities than the Ag−pSi, respectively. For the (−) charged FL, the Ag−pSi demonstrates 10 times higher intensity than the Ag−nSi. The intensity of the SERS as a function of the dye concentration shows that the detection limit differs by 10^2−10^9 M for the (+)/(−) charged dyes, confirming their excellent charge selectivity (see SI, Figure S5 and Table S1). It is noteworthy that the Si NWs induce the higher sensitivity and charge selectivity than the graphitic layer sheathed NWs. However, the Si NW substrates usually degrade the SERS signal more quickly than the graphitic layer shells for high intensity laser irradiation, thus demonstrating a significant advantage for the graphitic shell in terms of its photostability. In the case of Au−pSi and Au−nSi, the SERS

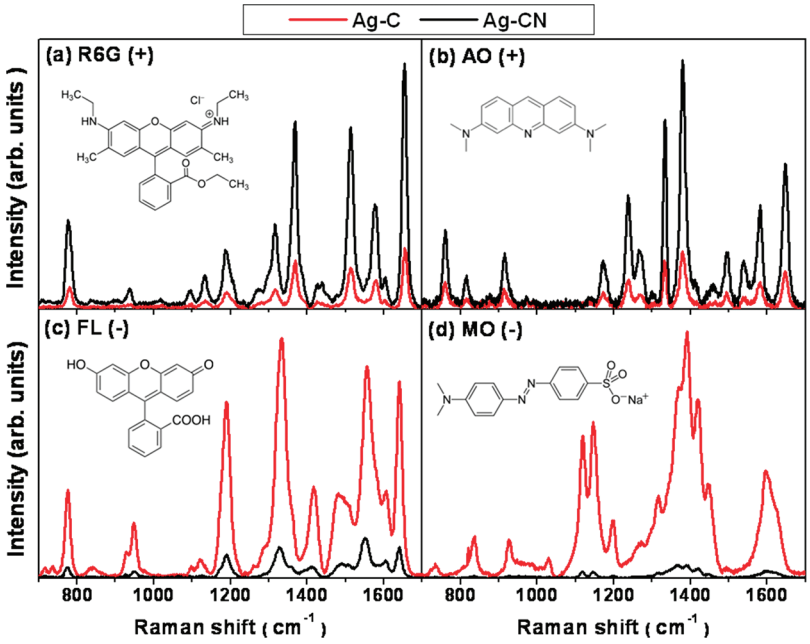

Figure 2. SERS of (a) R6G (+), (b) AO (+), (c) FL (−), and (d) MO (−) dyes for the Ag−C and Ag−CN, recorded under the same conditions where the concentration is 10^{-6} M. Molecular structures of dyes are drawn. The excitation wavelength is 514.5 nm from an Ar ion laser.

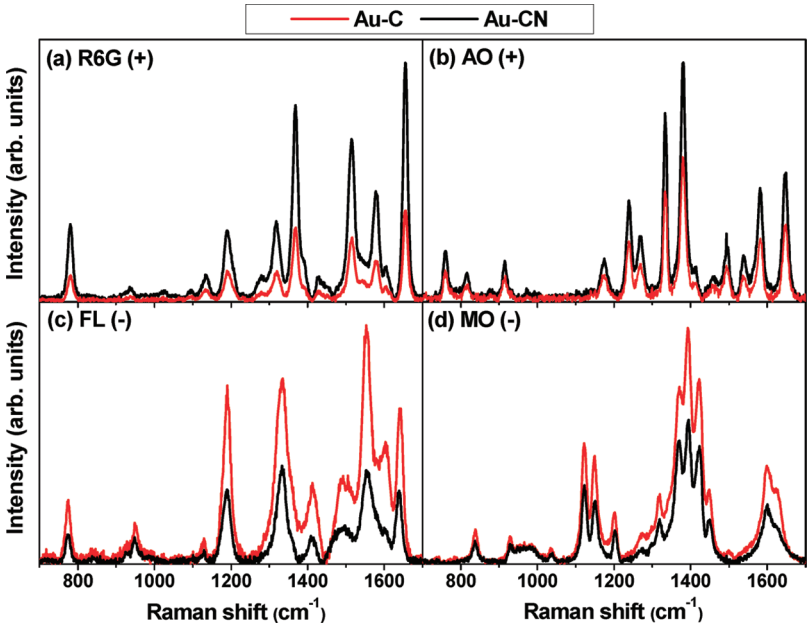

Figure 3. SERS of (a) R6G (+), (b) AO (+), (c) FL (−), and (d) MO (−) dyes for the Au−C and Au−CN, recorded under the same conditions where the concentration is 10^{-6} M. The excitation wavelength is 514.5 nm from an Ar ion laser.

shows much less charge selectivity than that of the Ag NPs (SI, Figures S6 and S7 and Table S1).

Figure 5 shows the histogram summarizing the relative intensity of SERS (dye concentration = 10^{-6} M) for all of the Ag and Au NP deposited NW substrates. The intensity is normalized relative to the maximum peak intensity of the paired substrates. For both the Ag and Au NPs, the N-doped graphitic layer consistently induces a higher sensitivity toward the (+) charged dyes than the undoped ones. The undoped graphitic layers show excellent selectivity toward the (−) charged dyes. The Ag NPs demonstrate more distinctive charge selectivity than the Au NPs. The Ag deposited p-type and n-type Si NWs exhibit very good charge selectivity toward the (−) and (+) dyes, respectively. In contrast, the Au deposited Si NWs show much less charge selectivity. In addition, we measured the SERS using the different length (2−7 μm) of NW, as shown in the SI, Figure S8. The sensitivity reaches a maximum at 7 μm, and the charge selectivity appears independently

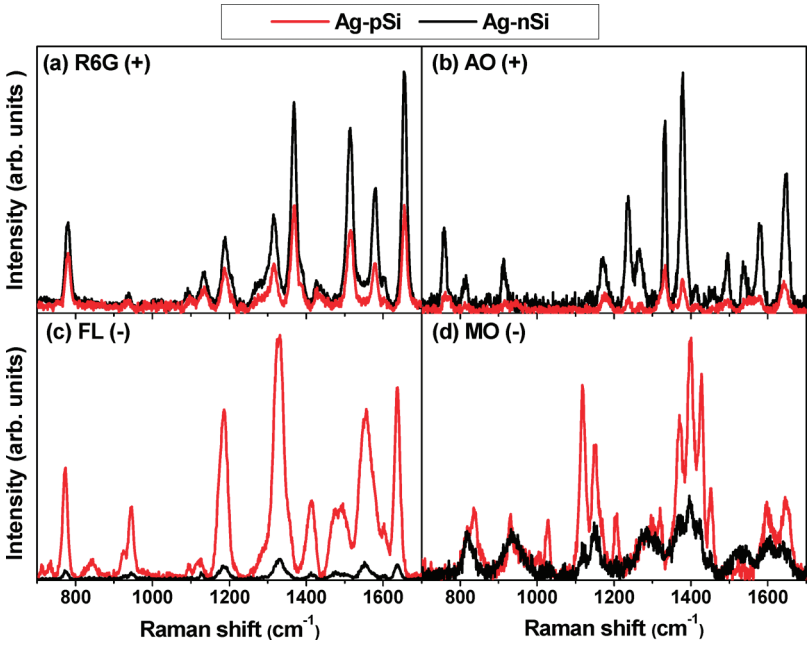

Figure 4. SERS of (a) R6G (+), (b) AO (+), (c) FL (−), and (d) MO (−) dyes for the Ag−pSi and Ag−nSi, recorded under the same conditions where the concentration is 10^{-6} M. The excitation wavelength is 514.5 nm from an Ar ion laser.

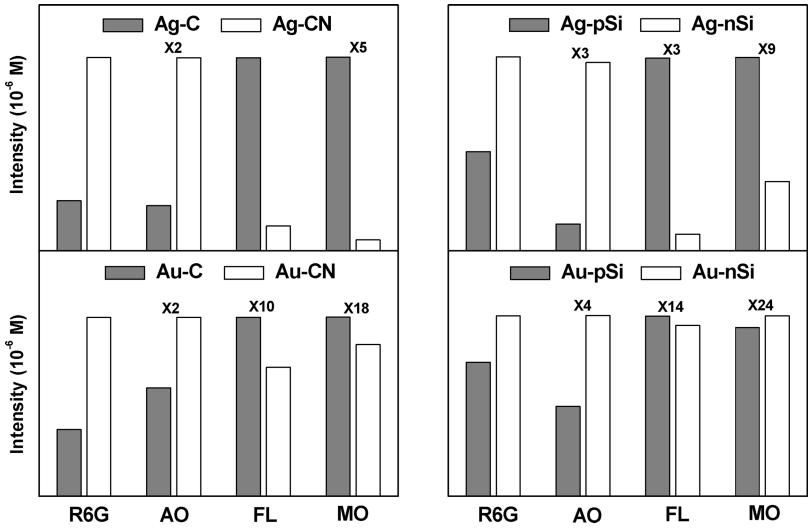

Figure 5. Histogram showing the relative sensitivity of SERS for the Ag and Au NP deposited NW substrates. The SERS intensity is normalized relative to the maximum intensity of the paired substrates.

on the NW length. This observation leads us to conjecture that the charge selectivity mainly originates from the different degrees of electrostatic interaction of the charged dyes with the metal NPs which, in turn, are determined by the charge transfer between the substrates and metal NPs.

XPS of Ag and Au Deposited Si−C Core−Shell NWs. Figure 6a displays the fine-scanned XPS Ag $3d_{5/2}$ peaks of the Ag−C and Ag−CN samples. The Ag NPs on the undoped graphitic layers show a peak at 368.4 eV, which is slightly blue-shifted from that of the bulk metal (368.3 eV). The absence of any peaks in the higher energy region confirms that oxide-free Ag NPs are produced using our SILA method. The peak of the Ag−CN is shifted to the lower energy region by 0.3 eV, compared to that of the bulk metal; 0.4 eV red shifts from that of the Ag−C. The peak of the Ag−CN is broader than that of the Ag−C; the full width at half-maximum values are 0.7 and 0.85 eV for Ag−C and Ag−CN, respectively. Figure 6b corresponds to the fine-scanned Au $4f_{7/2}$ peaks of the Au−C and Au−CN. The Au NPs on the undoped graphitic layers exhibit a peak at 83.9 eV, which is slightly red-shifted (0.1 eV) from that of the bulk metal (84.0 eV). The N doping of the graphitic layers induces a large red shift of 0.3 eV from that of the bulk metal (0.2 eV from that of the

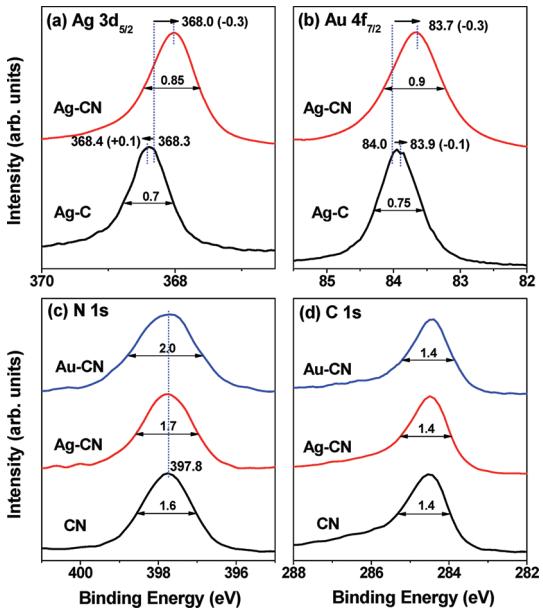

Figure 6. XPS data of Ag NPs and Au NPs deposited on the undoped (C) and N-doped graphitic layers (CN); (a) Ag $3d_{5/2}$, (b) Au $4f_{7/2}$, (c) N 1s, and (d) C 1s.

undoped one) and more peak broadening (*i.e.*, the fwhm values are 0.75 and 0.9 eV for Au−C and Au−CN, respectively).

The larger red shift of the Ag−CN and Au−CN (compared to that of the undoped ones) might be related to the increased electron density due to the more effective electron donation from the N-doped graphitic layers to the NPs. Their broader binding energy distribution is also attributed to the stronger interaction with the N-doped graphitic layers, accompanying the electron transfer. The N doping induces the larger red shift (0.4 eV relative to the undoped one) for the Ag NPs, compared to the Au NPs (0.2 eV), which also correlated with the more effective electron donation to the Ag NPs. We measured the XPS Ag 3d and Au 4f peaks for the Ag−Si and Au−Si and discussed their peak shift and broadening, as shown in the SI, Figure S9.

Figures 6c displays the fine-scanned N 1s peak of the N-doped samples before and after the deposition of the NPs, respectively. The survey spectrum confirmed the incorporation of 30% N atoms into the graphitic layers. The N 1s peak was centered at 397.8 eV for all three samples. We assigned it to the pyridine-like structure, consistently with our previous studies.[35] We also reported that, as the content of N increases, the pyridine-like form becomes dominant.[35] At a N doping level as high as 30%, only pyridine-like structures are formed. The fwhm values are 1.6, 1.7, and 2.0 eV for CN (before NP deposition), Ag−CN, and Au−CN, respectively. Figure 6d displays the fine-scanned C 1s peaks of the CN, Ag−CN, and Au−CN. The peak broadening is less sensitive to the metal deposition compared to that of the N 1s peak. The broadening of the N 1s peak is attributed to the interaction of the graphitic π bonding electrons with the metal NPs. For the pyridine molecules adsorbed on the Ag_n clusters, the coordinate bond of N→Ag *via* the lone pair electron of N atoms was theoretically predicted.[39] In the present case, the lone pair electrons of the pyridine-like N atoms are located in the plane of the graphitic layers and parallel to the metal NP surface (*i.e.*, flat lying configuration).[40] Therefore, we simply infer that they may not be involved in such a coordination interaction (*i.e.*, stand up configuration). Nevertheless, our quantum mechanical calculation suggests the possibility of a coordinate bond being formed between the N atoms and the metal NPs, as will be discussed later.

Doping Effect of the Pyridine-like N Structures and the Metal NPs on the Graphitic Layers. The band structures of both pristine multiwalled CNTs and graphene have zero band gap and usually show p-type doping behavior, due to the absorption of oxygen or water in the air.[41−45] The N-doped ones typically exhibit n-type semiconductor behavior since the substituted N atoms can introduce strong electron donor states near the Fermi level, corresponding to a reduction in the work function. Recent experimental works on graphene consistently showed that N doping enhanced the field emission performance, electrocatalytic activity, and charge capacity.[46−53]

The incorporation of N atoms produces two major N structures; one is a substitutional graphite-like structure, and the other is a pyridine-like defect structure. The pyridine-like structures are generally characterized as *vacancy sites*, formed in such a way that three or four C dangling bonds at adjacent sites are substituted by N atoms.[35,54,55] In the case of CNTs, it was pointed out that the graphite-like structure enhances the field emission properties, whereas the defective pyridine-like structure degrades them.[56,57] However, the electrocatalytic activity and lithium ion charge capacity of the pyridine-like structure are superior to those of the graphite-like structure.[58,59]

Czerw *et al.* predicted that the pyridine-like structures of MWCNTs produce strongly localized donor-like states just above the Fermi level (0.2 eV for 5.5% N substitution) using tight binding *ab initio* calculations.[54] The n-type doping effect of the pyridine-like structures of graphene and CNTs was further confirmed by a number of experimental and theoretical works.[60−62] The UV photoelectron spectra (UPS) of the N-doped (pyridine-like) graphene and MWCNTs (graphite- and pyridine-like mixture) revealed that 16 and 12% N substitution reduced the work function by 0.2 and 0.5 eV, respectively.[49,63] The valence band region of the XPS spectra also showed that the pyridine-like N structure induces a higher density of states in the vicinity of the Fermi level, corresponding to the n-type doping effect.[64] On the contrary, some calculations showed that the graphite-like CNTs are n-type doped ones, whereas the pyridine configuration introduces

no appreciable doping effect or, indeed, p-type doping effect.[55,65,66]

In order to examine whether the N doping induces the charge-selective SERS, we measured the SERS of four charged dyes without the deposition of the metal NPs and observed that the N doping diminishes the fluorescence of the dye (SI, Figure S10). However, the dyes without metal NPs show very little charge selectivity and much lower sensitivities than those of the metal NP deposited ones. The Zhang group reported that the Raman scattering intensity of metal phthalocyanine molecules on graphene can be controlled by tuning the Fermi level of the latter; p-type doping leads to larger Raman signal enhancement, while n-type doping reduces it.[23] Yu *et al.* showed that oxidized graphene provides higher Raman enhancement than pristine graphene, suggesting a chemical enhancement mechanism in which the oxygen-containing functional groups have a larger polarizability and stronger local dipole moment.[22] These works provide hints that the n-type doping and chemical enhancement have opposite effects on the SERS intensity. On the other hand, it was reported that the Raman enhancement of graphene is reduced as the number of layers increases.[20] Therefore, the negligible charge selectivity of our graphitic layers can be attributed to these complicated enhancement factors, as well as the large number of graphene sheets.

Giovannetti *et al.* reported a theoretical study that shows the effect of the n-type and p-type doping of Ag (work function = 4.3 eV) and Au (work function = 5.1 eV) metals on graphene (work function = 4.5 eV), respectively, due to the electron transfer from the lower to higher work function material.[67] Shin and co-workers suggested that the deposition of Ag and Au on graphene induces n- and p-type doping, respectively, using Raman spectroscopy.[28] Later, Han and co-workers claimed that the strain effect rather than the charge transfer is responsible for the Raman peak shift.[68] Huh *et al.* reported the n-type doping of graphene covered with patterned Au NPs using electron transport measurements.[69] Therefore, the effect of doping of the metal NPs on the nanosize graphite sheets remain as unanswered questions.

The deposition of metal NPs on the undoped and pyridine-like N-doped graphitic layer structures allows us to compare their doping effect. The XPS peak shift suggests the transfer of electrons to the Ag and Au NPs for the pyridine-like structures, corresponding to the p-type doping effect. It also indicates the transfer of electrons from the Ag NPs to the undoped graphitic layers (n-type doping effect) and the opposite effect for the Au NPs (p-type doping effect). The doping effect of the metal NPs may be responsible for their SERS charge selectivity; the electron transfer owing to their p-type doping effect produces more (−) charged metal NPs and, thus, the (+) charge selectivity of SERS.

TABLE 1. Parameters of Graphene−Ag and Graphene−Au Adducts, Calculated Using First Principles Calculations

metal	graphene	C_N (%)[a]	E_b (eV)[b]	R (Å)[c]	ΔE_F (eV)[d]
Ag(111)	Gr	0	−1.01	3.29	0.28
	N-Gr	3.13	−1.08	3.29	−0.09
	P-Gr	13.33	−1.38	2.45, 3.06	0.77
Au(111)	Gr	0	−1.06	3.37	−0.29
	N-Gr	3.13	−1.42	3.37	−0.20
	P-Gr	13.33	−1.07	2.80, 3.25	0.39

[a] Concentration of the doped N atoms. [b] Binding energy of the graphene with the metal surface. [c] Graphene−metal interplanar separation. For P-Gr, two numbers appear because its two N atoms are closer to the metal surface than the other atoms, due to the distortion of the geometry. See the text for more details. [d] Fermi level shift with respect to that of the free-standing graphene upon its adsorption on the metal surface.

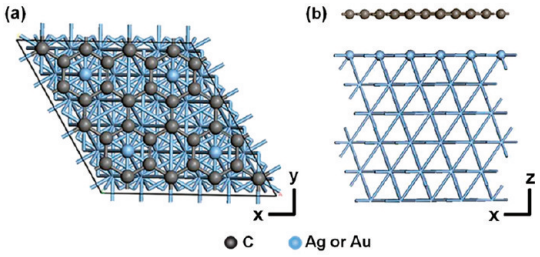

Figure 7. Molecular structure of the undoped Gr adsorbed on the Ag(111) or Au(111) surfaces, with the (a) top and (b) side views. The atoms belonging to the Gr and the topmost layer of the metal are shown in the ball-and-stick model, while the other Ag atoms are shown in the stick model.

Graphene−metal Adducts Using First Principles Calculations. In order to explain the electron-donating capacity of the N-doped graphitic layers to the metal NPs (p-type effect), we examined the electronic structure of the graphene adsorbed on the Ag(111) and Au(111) surfaces, using the first principles method. Table 1 lists the parameters of the most stable configuration of graphene−metal adducts.

Figure 7 shows the configuration of the graphene (denoted as Gr) on the 4 × 4 Ag(111) or Au(111) metal surface; eight carbon atoms of the Gr were located on top of the Ag atoms, while the other 24 atoms were placed in the hollow sites. The binding energy is calculated to be 1.01 and 1.06 eV for Ag and Au, respectively. We calculated the p_z component of the partial density of states (PDOS) summed over all of the atoms belonging to the free-standing undoped Gr and their metal adduct. The upward shift (0.28 eV) of the Fermi level of the Gr−Ag adduct clearly indicates the n-type doping effect of the adsorption of Ag on the Gr, which is consistent with a previous work.[68] In contrast, the Gr−Au adduct shows a downward shift (−0.29 eV) of the Fermi level, corresponding to the p-type doping effect. Our separate calculation shows that the work function of the undoped graphene is 4.48 eV, which is in good agreement with a recent experimental result (4.57 eV).[70] If the work functions (or Fermi levels) of the

Ag and Au NPs are similar to those of the bulk, viz. 4.3 and 5.1 eV, respectively, the n-type (Ag) and p-type (Au) doping effect can be suitably explained in terms of the alignment of the Fermi level upon the formation of the adduct. Under ambient conditions, the adsorption of oxygen molecules lowers the work function and further enhances the n-type doping effect of the Ag NPs.

For the N-doped graphene, we consider both the graphitic-like (denoted as N-Gr) and pyridine-like (denoted as P-Gr) structures. In the N-Gr, one C atom among the 32 atoms was substituted by a N atom, which corresponds to a doping concentration of 3.13%. Two different configurations (A and B) of the (N-Gr)−Ag (or Au) adduct are possible, as shown in Figure 8. Configurations A and B are characterized by the presence of the N atoms in the hollow sites or top sites, respectively. Configuration A is more stable than configuration B by 0.02 eV for both Ag(111) and Au(111). The binding energies of configuration A are 1.08 and 1.42 eV for Ag and Au, respectively, indicating that the N doping enhances the bonding interaction with the metal. Figure S11 (SI) gives a comparison of the p_z component of PDOS summed over all of the graphene atoms of the free-standing N-Gr with that of the (N-Gr)−metal adduct. The adsorption on the Ag(111) or Au(111) surface clearly exhibits a p-type doping effect; the Fermi level shifts downward by −0.09 and −0.20 eV for Ag and Au, respectively.

The 13.33% N-doped P-Gr was modeled by a graphene sheet with four N atoms around two vacancy sites.[35,54,55] Figure 9 displays configurations A and B of the (P-Gr)−Ag adduct. In configuration A, six C atoms and two N atoms are located above the Ag atoms of the topmost layer, which is more stable than configuration B by 0.22 eV. The two Ag−N bond distances (2.45 Å) are significantly shorter than the interplanar separation (3.06 Å) at the other atoms which are not directly involved in the bond formation, causing the deformation of the graphene plane. The side view clearly shows a reduction in the distance between the N and Ag atoms. It is worth mentioning that the Ag−N distance is comparable to those (2.26−2.46 Å) in the complex of Ag_n (n = 2−20) clusters and pyridine.[39] The binding energy of the (P-Gr)−Ag adduct is 1.38 eV, which is appreciably larger than that of the Gr−Ag one (1.01 eV). The PDOS analysis of the (P-Gr)−Ag adduct at various interplanar separations seems to show a gradual upward shift of the Fermi level as the P-Gr approaches the Ag(111) surface along the vertical direction (see SI, Figure S12). At the equilibrium separation, the shifts are 0.77 and 0.39 eV for Ag and Au, respectively. In fact, the work function (4.91 eV) of the P-Gr is larger than that of the undoped Gr, which is consistent with previous theoretical works.[65,66] These results are *apparently* inconsistent with the direction of charge transfer which would be expected from our (+) charge selective SERS. However, it should be

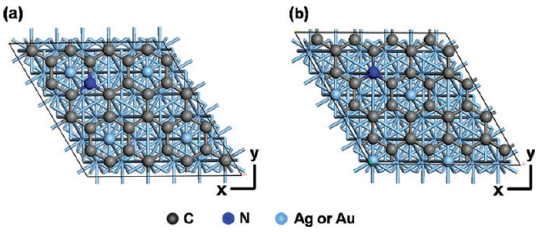

Figure 8. Molecular structures of configurations (a) A and (b) B of (N-Gr)−Ag (or −Au) adduct.

mentioned that this kind of simple analysis based on the Fermi level alignment can be misleading when chemical bonds are formed at the interface.

We recall that the binding energy of the (P-Gr)−Ag adduct (1.38 eV) is much larger than those of the Gr−Ag (1.01 eV) or (N-Gr)−Ag (1.08 eV) ones, and the Ag−N distances are considerably shorter than the interplanar separations of the undoped Gr and N-Gr adducts. The additional Mulliken charge analysis shows that there is a net transfer of 0.29 and 0.40 electrons from the P-Gr to the Ag(111) and Au (111)surfaces, respectively. In the case of N-Gr, there are net transfers of 0.74 and 0.70 electrons from the N-Gr to the Ag(111) and Au(111) surfaces, respectively. Namely, both P-Gr and N-Gr suffer from the p-type doping effect of the metal NPs. Herein, we suggest the formation of N→Ag coordinate bonds along the direction perpendicular to the graphene plane, which is known to occur only when the lone pair electrons are directed along the parallel direction, as in the pyridine−Ag_n complex.[39]

Consistent with the coordinate bond formation, we confirmed that the transferred electrons mostly occupy the Ag p_z orbital of the topmost layer. In addition, the Ag adsorption brings about an electronic reconfiguration of the N_{Ag} atom in which a small proportion (0.07 electrons) of the lone pair electrons in the p_x or p_y orbital becomes a p_z electron and reinforces the N→Ag bond. [Here, N_{Ag} denotes an N atom directly involved in the N→Ag bond.] The corresponding rearrangement is significantly smaller for the (N-Gr)−Au (0.03 electrons) and (N-Gr)−Au (or −Ag) (≤0.01 electrons) adducts. Therefore, the overall charge transfer to the metal can be understood to take place *via* two competing mechanisms. First, electron transfer occurs from the Ag to the P-Gr in such a way that they acquire a common Fermi level. Second, the N→Ag coordinate bond formation at the interface brings about the transfer of electrons in the reverse direction, which leads to the accumulation of a (−) charge on the Ag NPs. The Mulliken charge of Au (0.40 electrons) corresponds to a p-type doping effect like that in the Gr−Au. The binding energy of (P-Gr)−Au (1.07 eV) is nearly the same as that of Gr−Au (1.06 eV). This explains why the charge selectivity of the Au NPs is much weaker than that of the Ag NPs.

Electron Transfer Model for Charge-Selective SERS. Figure 10 shows a schematic diagram for our electron transfer

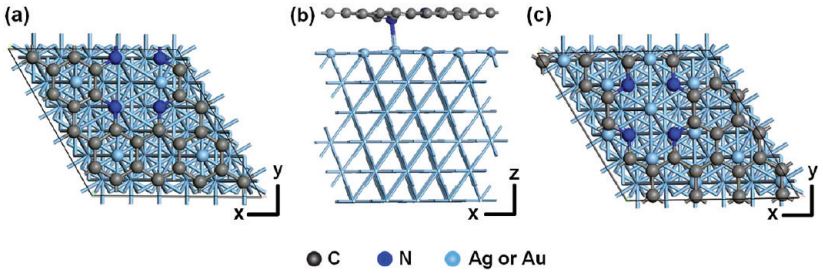

Figure 9. Molecular structures of configurations (a), (b) A and (c) B of (P-Gr)–Ag (or –Au) adduct. The side view of configuration A indicates the formation of two Ag–N bonds.

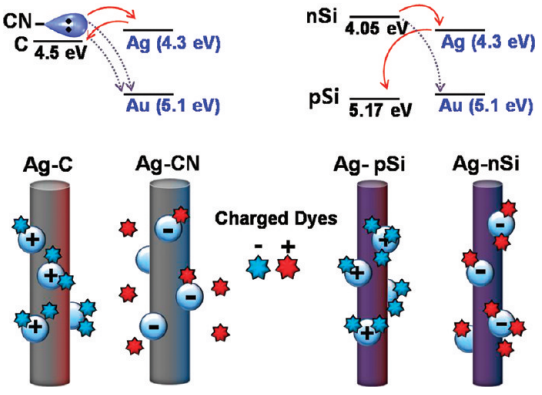

Figure 10. Schematic diagram for the electron transfer model of (a) Ag–C, Ag–CN, Au–C, and Au–CN; (b) Ag–pSi, Ag–nSi, Au–pSi, and Au–nSi.

model. The work function of the metal NPs is assumed to be the same as that of the bulk. The work function of the graphitic layers is approximated as that of graphene (4.5 eV). The XPS data revealed more efficient electron transfer to the NPs for the N-doped graphitic layers compared to the undoped ones. Our first principles calculation suggests that the lone pair electrons of the N atom transfer to the metal NPs by forming a coordinate bond, although the work function is 4.9 eV. Once electron transfer occurs from the N-doped graphitic layers, the NPs would be expected to be more (–) charged and prefer the adsorption of the (+) charged dye, resulting in a higher SERS intensity compared to that of the undoped graphitic layers. On the other hand, the adsorption of the (–) charged dye would be less favorable, due to the charge repulsion, producing a lower SERS intensity. When the Ag NPs donate electrons to the undoped graphitic layers owing to the difference of work function, distinctive (–) charge selectivity appears. In the case of Au NPs, both the undoped and N-doped graphitic layers can donate electrons to them (as marked by the dotted curved lines). The XPS peak analysis and the binding energy calculation support the less distinctive charge transfer of the N-doped graphitic layers, compared to the Ag NPs. As a result, their charge selectivity is expected to be weaker than that of the Ag NPs, which is coherent with the SERS results.

In contrast to the graphitic layers, the charge-selective SERS of Ag–pSi and Ag–nSi are essentially attributed to the difference in the work function (or Fermi level) between the Ag NPs and Si NWs. Bhatt *et al.* showed that Ag NPs on n- and p-type Si substrates exhibit enhanced SERS sensitivity toward (+) and (–) dye molecules, respectively.[17] They explained that the Fermi level (E_F) for heavily doped p- and n-type Si, E_F, can be approximated to be at the valence and conduction band edges, that is, –5.17 and –4.05 eV, respectively. The Ag NPs lose or gain electrons upon their contact with p- and n-type Si, resulting in (–) and (+) charge selectivity, respectively. The present result can be explained by the electron transfer in which the n-type Si donates electrons to the Ag NPs, while the p-type Si withdraws electrons from them, as shown by the schematic model (see Figure 10). To put it simply, the n-type Si donates more electrons to the Ag NPs than the p-type Si, which causes the more (–) charged Ag NPs to be sensitive to the (+) charged dye. In the case of the Au NPs, n-type Si donates electrons to the Au NPs, while p-type Si cannot accept effectively from them due to their similar work functions. Therefore, the charge selectivity is considerably reduced, which is consistent with the results obtained for Au–C and Au–CN.

CONCLUSIONS

We prepared eight types of highly sensitive SERS substrates; Ag or Au NP deposited Si–C core shell NWs with undoped and N-doped graphitic layers, viz. Ag–C, Ag–CN, Au–C, and Au–CN; Ag or Au NP deposited p-type and n-type Si NWs, viz. Ag–pSi, Ag–nSi, Au–pSi, and Au–nSi. The Ag or Au NPs were synthesized by a SILA method. The Si NWs were synthesized by the metal-assisted catalytic etching of a Si wafer, and the C shells were homogenously produced *via* the thermal CVD and doped with 30% pyridine-like N atoms. We demonstrated that the charge selectivity of SERS can be exclusively controlled by the doping of the Si and graphitic layers. The Ag–C and Ag–CN exhibit higher SERS intensity toward the (–) charged (FL and MO) and (+) charged dyes (R6G and AO), respectively. The Ag–pSi and Ag–nSi also exhibit excellent charge selectivity of SERS toward the (–) and (+) charge dyes,

respectively. The charge selectivity of the Ag NPs is higher than that of the Au NPs. The XPS peak analysis indicates that the N-doped graphitic layers donate more electrons to the metal NPs than the undoped ones, and electron transfer occurs to a greater extent for the Ag NPs than for the Au NPs.

We performed first principles calculations on the electronic structure of the undoped graphene and N-doped (graphite-like and pyridine-like) Gr sheets adsorbed on the Ag(111) and Au(111) surfaces. The binding energies of the Gr−metal adducts suggest that the large electron transfer capacity of the pyridine-like structures is due to the N→Ag coordinate bond formation involving the lone pair electrons of the N atoms. On the basis of the XPS results and calculations, we propose that the more (−) charged NPs on the N-doped graphitic layers facilitate the adsorption of the (+) charged dye, resulting in remarkable charge-selective SERS. The charge-selective SERS of Si NW substrates is basically attributed to the difference in the work function between the metal and Si; n-type Si donates more electrons to the Ag NPs than the p-type Si, which causes the more (−) charged Ag NPs to be sensitive to the (+) charged dye.

EXPERIMENTAL SECTION

Synthesis of Si NW and S−C Core−Shell NWs. The synthesis of the Si NW and graphitic layer deposited Si NW is described elsewhere.[35] Briefly, Si NWs were fabricated by metal-assisted chemical etching. The p-type and n-type (100) Si wafers (area = 2×2 cm^2), which are lightly doped with boron ($R = 1-20$ Ωcm) and phosphor ($R = 1-10$ Ωcm), respectively, were electrochemically etched using 4.8 M HF/0.005 M $AgNO_3$/0.4 M H_2O_2. After five etchings, the Si wafers were washed repeatedly with water and then immersed in dilute HNO_3 (1:1 v/v) to dissolve the Ag NP catalyst. The etched Si wafers were washed with 5% HF again to remove the oxide layer and cleaned with distilled water. The Si NWs were placed inside a CVD reactor tube, and a mixture of CH_4 and H_2 was introduced at flow rates of 50 and 100 sccm, respectively, for 20 min once the temperature reached 1000 °C. For the N-doped graphitic layers, NH_3 (flow rate = 100 sccm) was mixed with CH_4/H_2 at the same temperature.

Deposition of Metal NPs. The Ag NPs were deposited on the NWs by a SILAR method using $AgNO_3$ and ammonia borane (AB, NH_3BH_3) as the reducing reagent. In each cycle, the NW substrate was immersed in 0.01 M $AgNO_3$ aqueous (distilled water) solution for 30 s to ensure that a layer of Ag^+ ions was bonded on the surface of the NWs. The substrate was then rinsed with distilled water for 30 s to remove the weakly adsorbed ions and molecules. Afterward, the substrate was immersed in 0.01 M AB solution for 30 s, leading to the production of Ag, followed by rinsing in water. This process was repeated for 20 cycles. The deposition of the Au NPs was carried by the same SILAR procedure except that 0.01 M $HAuCl_4$ aqueous solution was used instead of $AgNO_3$.

Characterization. The products were analyzed by scanning electron microscopy (SEM, Hitachi S-4700), field-emission transmission electron microscopy (TEM, JEOL JEM 2100F and FEI TECNAI G^2 200 kV), high-voltage TEM (HVEM, JEOL JEM ARM 1300S, 1.25 MV), and energy-dispersive X-ray fluorescence spectroscopy (EDX). The Raman spectra were measured using the 514.5 nm line of an argon ion laser. X-ray photoelectron spectroscopy (XPS) was performed using the 8A1 beamline of the Pohang Light Source (PLS) and a laboratory-based spectrometer (ESCALAB 250, VG Scientifics) using a photon energy of 1486.6 eV (Al Kα).

SERS Measurements. Amounts of 10^{-4} to 10^{-10} M Rhodamine 6G (R6G), acridine orange (AO), fluorescein (FL), and methyl orange (MO) aqueous solutions were prepared. The substrates were immersed in the dye solution for 1 h. After drying, Raman spectroscopy measurements were performed on a home-built (equipped with a CCD camera) or HR-800 (HORIBA Jobin Yvon) Raman microscope using 514.5 or 633 nm laser radiation, respectively, with a power of 0.7−4 mW (514.5 nm) or 1−1.5 mW (633 nm) and integration time of 1−10 s.

First Principles Calculation. Geometric optimizations were carried out using the Vienna *ab initio* simulation package (VASP).[71] Electron−ion interactions were described by the projector-augmented wave (PAW) method, which is basically a frozen-core all-electron calculation.[72] All of the calculations were done employing the LDA exchange-correlation functional. We fix the lattice constant of 4×4 honeycomb Gr lattice in *XY* plane to its optimized value of 9.78 Å and adapt the lattice constant of the metal accordingly. This approximation is reasonable since the lattice constant mistamatch between graphene and metal is less than 2.8% for the Ag(111) and Au(111) surface. The metal NP was approximated by six (111) layers, and the nearest distance between two atoms along the direction perpendicular to the graphene plane is maintained to be larger than 13 Å. The *k*-point sampling was done with $15 \times 15 \times 1$ points in the first Brillouine zone. Mulliken population analysis was done using double-ζ double-polarized basis set in ATK 2010.02 program.[73]

Conflict of Interest: The authors declare no competing financial interest.

Acknowledgment. This study was supported by NRF (2011-001-5235; 2011-002-0090; 2011-001-9167; 2010-0007815), WCU (R31-000-10035-0), and KETEP (20104010100640). The HVEM (Daejeon) and XPS (Pusan) measurements were performed at the KBSI. The experiments at the PLS were partially supported by MOST and POSTECH. Computations were performed using a supercomputer at the Korea Institute of Science and Technology Information (KSC-2011-C1-11).

Supporting Information Available: SEM, TEM, XPS, SERS, and plots of the p_z component of PDOS are available. This material is available free of charge *via* the Internet at http://pubs.acs.org.

REFERENCES AND NOTES

1. Freeman, R. G.; Grabar, K. C.; Allison, K. J.; Bright, R. M.; Davis, J. A.; Guthrie, A. P.; Hommer, M. B.; Jackson, M. A.; Smith, P. C.; Walter, D. G.; *et al.* Self-Assembled Metal Colloid Monolayers: An Approach to SERS Substrates. *Science* **1995**, *267*, 1629–1632.
2. Kneipp, K.; Wang, Y.; Kneipp, H.; Perelman, L. T.; Itzkan, I.; Dasari, R. R.; Feld, M. S. Single Molecule Detection Using Surface-Enhanced Raman Scattering (SERS). *Phys. Rev. Lett.* **1997**, *78*, 1667–1670.
3. Nie, S.; Emory, S. R. Probing Single Molecules and Single Nanoparticles by Surface-Enhanced Raman Scattering. *Science* **1997**, *275*, 1102–1106.
4. Campion., A.; Kambhampati, P. Surface-Enhanced Raman Scattering. *Chem. Soc. Rev.* **1998**, *27*, 241–250.
5. Michaels, A. M.; Nirmal, M.; Brus, L. E. Surface-Enhanced Raman Spectroscopy of Individual Rhodamine 6G Molecules on Large Ag Nanocrystals. *J. Am. Chem. Soc.* **1999**, *121*, 9932–9939.
6. Chattopadhyay, S.; Lo, H.-C.; Hsu, C.-H.; Chen, L.-C.; Chen, K.-H. Surface-Enhanced Raman Spectroscopy Using Self-Assembled Silver Nanoparticles on Silicon Nanotips. *Chem. Mater.* **2005**, *17*, 553–559.
7. Qiu, T.; Wu, X. L.; Shen, J. C.; Ha, P. C. T.; Chu, P. K. Surface-Enhanced Raman Characteristics of Ag Cap Aggregates on Silicon Nanowire Arrays. *Nanotechnology* **2006**, *17*, 5769–5772.

8. Fan, J.-G.; Zhao, Y.-P. Gold-Coated Nanorod Arrays as Highly Sensitive Substrates for Surface-Enhanced Raman Spectroscopy. *Langmuir* **2008**, *24*, 14172–14175.
9. Zhang, B.; Wang, H.; Lu, L.; Ai, K.; Zhang, G.; Cheng, X. Large-Area Silver-Coated Silicon Nanowire Arrays for Molecular Sensing Using Surface-Enhanced Raman Spectroscopy. *Adv. Funct. Mater.* **2008**, *18*, 2348–2355.
10. Becker, M.; Sivakov, V.; Andrä, G.; Geiger, R.; Schreiber, J.; Hoffmann, S.; Michler, J.; Milenin, A. P.; Werner, P.; Christiansen, S. H. The SERS and TERS Effects Obtained by Gold Droplets on Top of Si Nanowires. *Nano Lett.* **2007**, *7*, 75–80.
11. Zhao, X.; Zhang, B.; Ai, K.; Zhang, G.; Cao, L.; Liu, X.; Sun, H.; Wang, H.; Lu, L. Monitoring Catalytic Degradation of Dye Molecules on Silver-Coated ZnO Nanowire Arrays by Surface-Enhanced Raman Spectroscopy. *J. Mater. Chem.* **2009**, *19*, 5547–5553.
12. Deng, S.; Fan, H. M.; Zhang, X.; Loh, K. P.; Cheng, C.-L.; Sow, C. H.; Foo, Y. L. An Effective Surface-Enhanced Raman Scattering Template Based on a Ag Nanocluster-ZnO Nanowire Array. *Nanotechnology* **2009**, *20*, 175705.
13. Chen, L.; Luo, L.; Chen, Z.; Zhang, M.; Zapien, J. A.; Lee, C. S.; Lee, S. T. ZnO/Au Composite Nanoarrays as Substrates for Surface-Enhanced Raman Scattering Detection. *J. Phys. Chem. C* **2010**, *114*, 93–100.
14. Chu, H.; Wang, J.; Ding, L.; Yuan, D.; Zhang, Y.; Liu, J.; Li, Y. Decoration of Gold Nanoparticles on Surface-Grown Single-Walled Carbon Nanotubes for Detection of Every Nanotube by Surface-Enhanced Raman Spectroscopy. *J. Am. Chem. Soc.* **2009**, *131*, 14310–14316.
15. Sun, Y.; Liu, K.; Miao, J.; Wang, Z.; Tian, B.; Zhang, L.; Li, Q.; Fan, S.; Jiang, K. Highly Sensitive Surface-Enhanced Raman Scattering Substrate Made from Superaligned Carbon Nanotubes. *Nano Lett.* **2010**, *10*, 1747–1753.
16. Dawson, P.; Duenas, J. A.; Boyle, M. G.; Doherty, M. D.; Bell, S. E. J.; Kern, A. M.; Martin, O. J. F.; Teh, A.-S.; Teo, K. B. K.; Milne, W. I. Combined Antenna and Localized Plasmon Resonance in Raman Scattering from Random Arrays of Silver-Coated, Vertically Aligned Multiwalled Cabon Nanotubes. *Nano Lett.* **2011**, *11*, 365–371.
17. Bhatt, K.; Tan, S.; Karumuri, S.; Kalkan, A. K. Charge-Selective Raman Scattering and Fluorescence Quenching by "Nanometal On Semiconductor" Substrates. *Nano Lett.* **2010**, *10*, 3880–3887.
18. Panarin, A. Y.; Terekhov, S. N.; Kholostov, K. I.; Bondarenko, V. P. SERS-Active Substrates Based on n-Type Porous Silicon. *Appl. Surf. Sci.* **2010**, *256*, 6969–6976.
19. Xie, L. M.; Ling, X.; Fang, Y.; Zhang, J.; Liu, Z. F. Graphene as a Substrate To Suppress Fluorescence in Resonance Raman Spectroscopy. *J. Am. Chem. Soc.* **2009**, *131*, 9890–9891.
20. Ling, X.; Xie, L. M.; Fang, Y.; Xu, H.; Zhang, H. L.; Kong, J.; Dresselhaus, M. S.; Zhang, J.; Liu, Z. F. Can Graphene Be Used As a Substrate for Raman Enhancement? *Nano Lett.* **2010**, *10*, 553–561.
21. Jung, N.; Crowther, A. C.; Kim, N.; Kim, P.; Brus, L. Raman Enhancement on Graphene: Adsorbed and Intercalated Molecular Species. *ACS Nano* **2010**, *4*, 7005–7013.
22. Yu, X.; Cai, H.; Zhang, W.; Li, X.; Pan, N.; Luo, Y.; Wang, X.; Hou, J. G. Tuning Chemical Enhancement of SERS by Controlling the Chemical Reduction of Graphene Oxide Nanosheets. *ACS Nano* **2011**, *5*, 952–958.
23. Xu, H.; Xie, L.; Zhang, H.; Zhang, J. Effect of Graphene Fermi Level on the Raman Scattering Intensity of Molecules on Graphene. *ACS Nano* **2011**, *5*, 5338–5344.
24. Huh, S.; Park, J.; Kim, Y. S.; Kim, K. S.; Hong, B. H.; Nam, J. M. UV/Ozone-Oxidized Large-Scale Graphene Platform with Large Chemical Enhancement in Surface-Enhanced Raman Scattering. *ACS Nano* **2011**, *5*, 9799–9806.
25. Gao, L.; Ren, W.; Liu, B.; Saito, R.; Wu, Z. S.; Li, S.; Jiang, C.; Li, F.; Cheng, H. M. Surface and Interference Coenhanced Raman Scattering of Graphene. *ACS Nano* **2009**, *3*, 933–939.
26. Xu, C.; Wang, X. Fabrication of Flexible Metal-Nanoparticle Films Using Graphene Oxide Sheets as Substrates. *Small* **2009**, *5*, 2212–2217.
27. Schedin, F.; Lidorikis, E.; Lombardo, A.; Kravets, V. G.; Geim, A. K.; Grigorenko, A. N.; Novoselov, K. S.; Ferrari, A. C. Surface-Enhanced Raman Spectroscopy of Graphene. *ACS Nano* **2010**, *4*, 5617–5626.
28. Lee, J.; Novoselov, K. S.; Shin, H. S. Interaction between Metal and Graphene: Dependence on the Layer Number of Graphene. *ACS Nano* **2011**, *5*, 608–612.
29. Fu, X. Q.; Bei, F. L.; Wang, X.; O'Brien, S.; Lombardi, J. R. Excitation Profile of Surface-Enhanced Raman Scattering in Graphene–Metal Nanoparticle Based Derivatives. *Nanoscale* **2010**, *2*, 1461–1466.
30. Goncalves, G.; Marques, P. A. A. P.; Granadeiro, C. M.; Nogueira, H. I. S.; Singh, M.; Gracio, J. Surface Modification of Graphene Nanosheets with Gold Nanoparticles: The Role of Oxygen Moieties at Graphene Surface on Gold Nucleation and Growth. *Chem. Mater.* **2009**, *21*, 4796–4802.
31. Wang, Y.; Ni, Z.; Hu, H.; Hao, Y.; Wong, C. P.; Yu, T.; Thong, J. T. L.; Shen, Z. X. Gold on Graphene as a Substrate for Surface Enhanced Raman Scattering Study. *Appl. Phys. Lett.* **2010**, *97*, 163111–163113.
32. Huang, J.; Zhang, L.; Chen, B. A.; Ji, N.; Chen, F. H; Zhang, Y.; Zhang, Z. J. Nanocomposites of Size-Controlled Gold Nanoparticles and Graphene Oxide: Formation and Applications in SERS and Catalysis. *Nanoscale* **2010**, *2*, 2733–2738.
33. Zhang, Z.; Xu, F. G.; Yang, W. S.; Guo, M. Y.; Wang, X. D.; Zhanga, B. L.; Tang, J. L. A Facile One-Pot Method to High-Quality Ag-Graphene Composite Nanosheets for Efficient Surface-Enhanced Raman Scattering. *Chem. Commun.* **2011**, *47*, 6440–6442.
34. Ren, W.; Fang, Y.; Wang, E. A Binary Functional Substrate for Enrichment and Ultrasensitive SERS Spectroscopic Detection of Folic Acid Using Graphene Oxide/Ag Nanoparticle Hybrids. *ACS Nano* **2011**, *5*, 6425–6433.
35. Cho, Y. J.; Kim, H. S.; Baik, S. Y.; Myung, Y.; Jung, C. S.; Kim, C. H.; Park, J.; Kang, H. S. Selective Nitrogen-Doping Structure of Nanosize Graphitic Layers. *J. Phys. Chem. C* **2011**, *115*, 3737–3744.
36. Li, J. J.; Wang, Y. A.; Guo, W. Z.; Keay, J. C.; Mishima, T. D.; Johnson, M. B.; Peng, X. Large-Scale Synthesis of Nearly Monodisperse CdSe/CdS Core/Shell Nanocrystals Using Air-Stable Reagents *via* Successive Ion Layer Adsorption and Reaction. *J. Am. Chem. Soc.* **2003**, *125*, 12567–12575.
37. Lee, H.; Wang, M.; Chen, P.; Gamelin, D. R.; Zakeeruddin, S. M.; Grätzel, M.; Nazeeruddin, Md. K. Efficient CdSe Quantum Dot-Sensitized Solar Cells Prepared by an Improved Successive Ionic Layer Adsorption and Reaction Process. *Nano Lett.* **2009**, *9*, 4221–4227.
38. Park, H. K.; Yoon, J. K.; Kim, K. Novel Fabrication of Ag Thin Film on Glass for Efficient Surface-Enhanced Raman Scattering. *Langmuir* **2006**, *22*, 1626–1629.
39. Jensen, L.; Zhao, L. L.; Schatz, G. C. Size-Dependence of the Enhanced Raman Scattering of Pyridine Adsorbed on Ag_n ($n = 2-8, 20$) Clusters. *J. Phys. Chem. C* **2007**, *111*, 4756–4764.
40. Hahn, J. R.; Kang, H. S. Role of Molecular Orientation in Vibration, Hopping, and Electronic Properties of Single Pyridine Molecules Adsorbed on Ag(110) Surface: A Combined STM and DFT Study. *Surf. Sci.* **2010**, *604*, 258–264.
41. Xiao, K.; Liu, Y.; Hu, P.; Yu, G.; Sun, Y.; Zhu, D. n-Type Field-Effect Transistors Made of an Individual Nitrogen-Doped Multiwalled Carbon Nanotube. *J. Am. Chem. Soc.* **2005**, *127*, 8614–8617.
42. Wei, D.; Liu, Y.; Wang, Y.; Zhang, H.; Huang, L.; Yu, G. Synthesis of N-Doped Graphene by Chemical Vapor Deposition and Its Electrical Properties. *Nano Lett.* **2009**, *9*, 1752–1758.
43. Guo, B.; Liu, Q.; Chen, E.; Zhu, H.; Fang, L.; Gong, J. R. Controllable N-Doping of Graphene. *Nano Lett.* **2010**, *10*, 4975–4980.
44. Jin, Z.; Yao, J.; Kittrell, C.; Tour, J. M. Large-Scale Growth and Characterizations of Nitrogen-Doped Monolayer Graphene Sheets. *ACS Nano* **2011**, *5*, 4112–4117.
45. Zhang, C.; Fu, L.; Liu, N.; Liu, M.; Wang, Y.; Liu, Z. Synthesis of Nitrogen-Doped Graphene Using Embedded Carbon and Nitrogen Sources. *Adv. Mater.* **2011**, *23*, 1020–1024.
46. Soin, N.; Roy, S. S.; Roy, S.; Hazra, K. S.; Misra, D. S.; Lim, T. H.; Hetherington, C. J.; McLaughlin, J. A. Enhanced and Stable

Field Emission from *In Situ* Nitrogen-Doped Few-Layered Graphene Nanoflakes. *J. Phys. Chem. C* **2011**, *115*, 5366–5372.
47. Qu, L.; Liu, Y.; Baek, J.-B.; Dai, L. Nitrogen-Doped Graphene as Efficient Metal-Free Electrocatalyst for Oxygen Reduction in Fuel Cells. *ACS Nano* **2010**, *4*, 1321–1326.
48. Wang, Y.; Shao, Y.; Matson, D. W.; Li, J.; Lin, Y. Nitrogen-Doped Graphene and Its Application in Electrochemical Biosensing. *ACS Nano* **2010**, *4*, 1790–1798.
49. Luo, Z.; Lim, S.; Tian, Z.; Shang, J.; Lai, L.; MacDonald, B.; Fu, C.; Shen, Z.; Yu, T.; Lin, J. Pyridinic N-Doped Graphene: Synthesis, Electronic Structure, and Electrocatalytic Property. *J. Mater. Chem.* **2011**, *21*, 8038–8044.
50. Reddy, A. L. M.; Srivastava, A.; Gowda, S. R.; Gullapalli, H.; Dubey, M.; Ajayan, P. M. Synthesis of Nitrogen-Doped Graphene Films For Lithium Battery Application. *ACS Nano* **2010**, *4*, 6337–6342.
51. Wu, Z.-S.; Ren, W.; Xu, L.; Li, F.; Cheng, H.-M. Doped Graphene Sheets as Anode Materials with Superhigh Rate and Large Capacity for Lithium Ion Batteries. *ACS Nano* **2011**, *5*, 5463–5471.
52. Joeng, H. M.; Lee, J. W.; Shin, W. H.; Choi, Y. J.; Shin, H. J.; Kang, J. K; Choi, J. W. Nitrogen-Doped Graphene for High-Performance Ultracapacitors and the Importance of Nitrogen-Doped Sites at Basal Planes. *Nano Lett.* **2011**, *11*, 2472–2477.
53. Jeon, I.-Y.; Yu, D.; Bae, S.-Y.; Choi, H.-J.; Chang, D. W.; Dai, L.; Baek, J.-B. Formation of Large-Area Nitrogen-Doped Graphene Film Prepared from Simple Solution Casting of Edge-Selectively Functionalized Graphite and Its Electrocatalytic Activity. *Chem. Mater.* **2011**, *23*, 3987–3992.
54. Czerw, R.; Terrones, M.; Charlier, J.-C.; Blase, X.; Foley, B.; Kamalakaran, R.; Grobert, N.; Terrones, H.; Tekleab, D.; Ajayan, P. M.; *et al.* Identification of Electron Donor States in N-Doped Carbon Nanotubes. *Nano Lett.* **2001**, *1*, 457–460.
55. Kang, H. S.; Jeong, S. Nitrogen Doping and Chirality of Carbon Nanotubes. *Phys. Rev. B* **2004**, *70*, 233411(1−4).
56. Zhong, Z.; Lee, G. I.; Mo, C. B.; Hong, S. H.; Kang, J. K. Tailored Field-Emission Property of Patterned Carbon Nitride Nanotubes by a Selective Doping of Substitutional N(sN) and Pyridine-like N(pN) Atoms. *Chem. Mater.* **2007**, *19*, 2918–2920.
57. Ghosh, K.; Kumar, M.; Maruyama, T.; Ando, Y. Tailoring the Field Emission Property of Nitrogen-Doped Carbon Nanotubes by Controlling the Graphitic/Pyridinic Substitution. *Carbon* **2010**, *48*, 191–200.
58. Chen, Z.; Higgins, D.; Chen, Z. Nitrogen Doped Carbon Nanotubes and Their Impact on the Oxygen Reduction Reaction in Fuel Cell. *Carbon* **2010**, *48*, 3057–3065.
59. Cho, Y. J.; Kim, H. S.; Im, H.; Myung, Y.; Jung, G. B.; Lee, C. W.; Park, J.; Park, M.-H.; Cho, J.; Kang, H. S. Nitrogen-Doped Graphitic Layers Deposited on Silicon Nanowires for Efficient Lithium-Ion Battery Anodes. *J. Phys. Chem. C* **2011**, *115*, 9451–9457.
60. Lin, Y.-C.; Lin, C.-Y.; Chiu, P.-W. Controllable Graphene N-Doping with Ammonia Plasma. *Appl. Phys. Lett.* **2010**, *96*, 133110.
61. Zheng, B.; Hermet, P.; Henrard, L. Scanning Tunneling Microscopy Simulations of Nitrogen- and Boron-Doped Graphene and Single-Walled Carbon Nanotubes. *ACS Nano* **2010**, *4*, 4165–4173.
62. Casolo, S.; Martinazzo, R.; Tantardini, G. F. Band Engineering in Graphene with Superlattices of Substitutional Defects. *J. Phys. Chem. C* **2011**, *115*, 3250–3256.
63. Lim, S. H; Elim, H. I.; Gao, X. Y.; Wee, A. T. S.; Ji, W.; Lee, J. Y.; Lin, J. Electronic and Optical Properties of Nitrogen-Doped Multiwalled Carbon Nanotubes. *Phys. Rev. B* **2006**, *73*, 045402.
64. Choi, H. C.; Park, J.; Kim, B. Distribution and Structure of N Atom in Multiwalled Carbon Nanotubes Using Variable-Energy X-ray Photoelectron Spectroscopy. *J. Phys. Chem. B* **2005**, *109*, 4333–4340.
65. Lim, S. H.; Li, R.; Ji, W.; Lin, J. Effect of Nitrogenation on Single-Walled Carbon Nanotubes within Density Functional Theory. *Phys. Rev. B* **2007**, *76*, 195406.
66. Cruz-Silva, E.; López-Urías, F.; Muñoz-Sandoval, E.; Sumpter, B. G.; Terrones, H.; Charlier, J.-C.; Meunier, V.; Terrones, M. Electronic Transport and Mechanical Properties of Phosphorus- and Phosphorus−Nitrogen-Doped Carbon Nanotubes. *ACS Nano* **2009**, *3*, 1913–1921.
67. Giovannetti, G.; Khomyakov, P. A.; Brocks, G.; Karpan, V. M.; van den Brink, J.; Kelly, P. J. Doping Graphene with Metal Contacts. *Phys. Rev. Lett.* **2008**, *101*, 026803.
68. Wang, W. X.; Liang, S. H.; Yu, T.; Li, D. H.; Li, Y. B.; Han, X. F. The Study of Interaction between Graphene and Metals by Raman Spectroscopy. *J. Appl. Phys.* **2011**, *109*, 07C501.
69. Huh, S.; Park, J.; Kim, K. S.; Hong, B. H.; Kim, S. B. Selective n-Type Doping of Graphene by Photo-Patterned Gold Nanoparticles. *ACS Nano* **2011**, *5*, 3639–3644.
70. Yu, Y.-J.; Zhao, Y.; Ryu, S.; Brus, L. E.; Kim, K. S.; Kim, P. Tuning the Graphene Work Function by Electric Field Effect. *Nano Lett.* **2009**, *9*, 3430–3434.
71. Kresse, G.; Furthmüller, J. Efficient Iterative Schemes for *Ab Initio* Total-Energy Calculations Using a Plane-Wave Basis Set. *Phys. Rev. B* **1996**, *54*, 11169–11186.
72. Kresse, G.; Joubert, D. From Ultrasoft Pseudopotentials to the Projector Augmented-Wave Method. *Phys. Rev. B* **1999**, *59*, 1758–1175.
73. Atomistix Toolkit version 2010.02; Quantumwise A/S, www.quantumwise.com.